JOURNAL OF PROPULSION AND POWER
Vol. 19, No. 4, July–August 2003

Erosive Burning of Ammonium Perchlorate/Hydroxyl-Terminated-Polybutadiene Propellants Under Supersonic Crossflows

S. Krishnan*
Indian Institute of Technology Madras, Chennai 600036, India
and
K. K. Rajesh†
Birla Institute of Technology, Mesra, Ranchi 835215, India

An experimental procedure adopted for measuring the erosive burning in solid propellants under transonic and supersonic crossflow Mach numbers is explained. Three formulations of ammonium perchlorate/hydroxyl-terminated-polybutadiene propellants of different burning rates (6, 9, and 16 mm/s at 5 MPa) were used for the study. The study presents the erosive burning results for a range of crossflow Mach numbers from 0.8 to 1.7. Additionally, the adopted experimental procedure clearly demonstrates the choking station movement in grain ports of nozzleless motors. As observed under subsonic crossflow conditions, in supersonic conditions the following conditions hold: 1) The erosive burning effect increases with the increase in both pressure and free stream velocity of crossflow. 2) The propellants with lower normal-burning rates experience greater erosive burning than those with higher normal-burning rates. Negative erosive burning under supersonic crossflow velocities is identified at low pressures.

Introduction

THE term erosive burning refers to the dependence of the burning rate of a solid propellant on the crossflow velocity of combustion products. This dependence can be on many fluid dynamic properties of the crossflow, but the crossflow velocity is the most important one. Because of the erosive burning, the burning rate of a propellant gets modified from the value of the normal-burning rate r_0. The normal-burning rate (or the burning rate under zero crossflow) is given by,

$$r_0 = ap^n \tag{1}$$

where a is the preexponent factor, p the pressure, and n the combustion index. The modified burning rate includes the component of normal burning, as well as that of erosive burning. The erosive-burning effect is represented by the erosive-burning ratio term ε_b, which is the ratio of the burning rate under crossflow r and the normal-burning rate r_0; $\varepsilon_b \equiv r/r_0$.

The erosive-burning effect generally increases with the increase in both pressure and the freestream velocity of the crossflow.[1,2] The burning rate of a propellant increases beyond the normal-burning rate only when the crossflow velocity has a value greater than a certain threshold value.[3–8] At low crossflow velocities, below the threshold velocity, the burning rate may decrease compared to the normal-burning rate. This is known as negative erosive burning.[4–6,9] The erosive-burning effect increases with a decrease in propellant initial temperature, and, at constant crossflow velocity and pressure, this effect is independent of crossflow temperature.[4,7,9–12] The propellants with lower normal-burning rates experience a greater erosive-burning effect than those with higher normal-burning rates.[3,4,10,12] Studies on metal addition indicate very little effect on erosive burning.[13,14] Also, the erosive burning is independent of the composition of the crossflow.[11,15] Studies on composite propellants conclude that the erosive-burning effect increases with an increase in oxidizer-particle size[2,12] and is strongly influenced by the type of binders used in the formulation.[1,2,4,9,14,16]

Bulgakov et al.,[17] through a modeling effort, explain the negative erosive-burning phenomenon. A modeling study by Godon et al.[18] shows that the normal-burning rate of a particular propellant is the main parameter that influences the propellant's erosive-burning characteristics. King[19] describes the motor-design problems caused by erosive burning in the nozzled motors with high throat-to-port area ratios and the nozzleless motors. In addition, in agreement with the observation of Godon et al.,[18] King concludes that among the many factors that can affect erosive burning, the normal-burning rate is the most important parameter. Mukunda and Paul[20] analyzed the erosive-burning effect to extract the inherent single correlation in terms of new nondimensional parameters. They have shown that the erosive-burning ratios of different propellants could be brought into a single correlation with the assumption that the phenomenon is fluid dynamically controlled. They have considered the erosive-burning data of a wide range of propellants from double base to composite, at varying energy levels, and of different normal-burning rates. The suggested correlation is claimed to be valid within the experimental accuracy in burning-rate measurements.

Design of nozzleless motors, as well as high-performance nozzled motors and the related performance predictions, require a detailed knowledge of erosive burning under transonic and supersonic crossflow velocities. The available erosive-burning data for these high-velocity conditions are very limited. Only meager data could be found for transonic crossflow conditions below $M = 1$ and none were found for supersonic conditions. The present study details the results of erosive-burning measurements carried out at crossflow Mach numbers from 0.8 to 1.7. Unmetallized composite propellants, containing ammonium perchlorate (AP) and hydroxyl-terminated-polybutadiene (HTPB), and of three different normal-burning rates, were used for the study. As observed under subsonic crossflow

Presented as Paper 2001-3580 at the AIAA/ASME/SAE/ASEE 37th Joint Propulsion Committee Conference and Exhibit, 8–11 July 2001, Salt Lake City, Utah; received 4 June 2001; revision received 12 March 2003; accepted for publication 20 March 2003.

*Professor of Aerospace Engineering; currently Professor of Mechanical Engineering, Kyungpook National University, Taegu 702701, Republic of Korea; skrish@bh.knu.ac.kr. Associate Fellow AIAA.

†Assistant Professor, Department of Space Engineering and Rocketry; currently Postdoctoral Fellow, Faculty of Aerospace Engineering, Technion–Israel Institute of Technology, Haifa 32000, Israel.

conditions, in supersonic conditions the following conditions hold: 1) The erosive burning effect increases with the increase in both pressure and freestream velocity of a crossflow. 2) The propellants with lower normal-burning rates experience greater erosive burning than those with higher normal-burning rates. The study identifies the existence of negative erosive burning under supersonic crossflow conditions. Additionally, the followed experimental procedure facilitates the clear demonstration of choking station movement in grain ports of nozzleless motors.

Experimental Procedure

The erosive-burning test facility comprises a gas generator, a transition duct, and a test chamber (Fig. 1). The test-chamber assembly includes the chamber block, the test channel, the end-nozzle assembly, and the bleed-nozzle assembly (Fig. 1). For the nozzleless mode of operation, the end-nozzle assembly is not fitted. The chamber block, a heavy stainless-steel casting, accommodates an interchangeable two-dimensional test channel shown in Fig. 2. The slab of the cured propellant specimen is carefully prepared to be "square" on all corners. By the use of an epoxy adhesive, the slab of the specimen is fixed on to the inner surface of the test channel's bottom plate. A tapered leading edge, cast out of epoxy, is glued on to the front portion of the specimen. During curing of the epoxy adhesive, to prevent the lifting of the slab from the surface, a teakwood block running throughout the length of the channel is tightly placed. After the propellant slab is fixed, the flow channel is checked for the stipulated rectangular cross section from entry to exit. The stuck specimen slab has a constant thickness up to the geometric throat, which is 366 mm away from the leading edge. From the geometric throat, it has an angle of 8 deg of supersonic expansion for a length of 81 mm (Fig. 2). For the remaining test-channel length of 50 mm, the inhibitor thickness is 5 mm, and the constant area section without mass addition is for the balance. On assembly, the flatness of the test chamber (hence, the flatness of the specimen slab) along the axis and perpendicular to the axis is carefully maintained by the use of spirit level and reference markings on the walls of the test cell.

A pyrotechnic igniter, fitted at the head end of the gas generator, ignites the gas-generator grain. The gas generator, provides high-pressure combustion products when an eight-pointed neutral star grain is burnt in it. The hot combustion products from the gas generator are directed to the test chamber through the transition duct, which provides a two-dimensional rectangular flow into the test chamber. With a suitable nozzle in the bleed-nozzle assembly, a small amount of combustion product from the gas generator is bled off upstream of the leading edge. The bleed flow and the tapered leading edge ensure a smooth development of boundary layer from the beginning of the propellant specimen. The chamber block, receiving the combustion products from the test channel, ejects them supersonically into the atmosphere through its rectangular-port exit (Fig. 2). With these arrangements, the crossflow over the propellant specimen changes from a subsonic to a supersonic value.

Through a transparent polymethyl methacrylate (PMMA) window assembly that consists of an inner sacrificial layer and an outer permanent layer, the burning propellant specimen is viewed by a high-speed rotating-prism camera (HYCAM II) and an S-Video camera. The lens axes of the cameras are maintained perpendicular to the axis of the flow channel. The high-speed camera recordings are made at 500–1200 frames per second using a 200-ft, 500 ASA, Kodak color negative film. During the recording, calibrated time intervals of 10 ms are marked on the film by a light-emitting diode by successive bright spots. With these markings, the framing rates can be accurately found at all times of the camera recordings, during starting acceleration as well as steady speed.

The high-speed camera is focused on a field width of about 150 mm. Under the nozzleless mode of operation, this focused field starts from 297 mm from the leading edge. The field width covers three distinct regions of the crossflow: 1) the subsonic region just upstream of the geometric throat (accommodating the so-called transonic test station), 2) the geometric-throat station, and 3) the supersonic region just after the geometric throat (accommodating the supersonic test station) (Fig. 2). Within the focused field, two rectangular fluorescent stickers, each cut accurately to a size of 50×10 mm and of a different color, are stuck on to the outer surface of the PMMA permanent-layer just below the view of the propellant specimen. These stickers serve as calibration strips in every frame of the exposed film.

To start with, pressure ports of 1-mm diameter were provided. Because clogging of these ports was experienced during certain tests, the port diameters were enlarged to 2 mm. The pressure ports

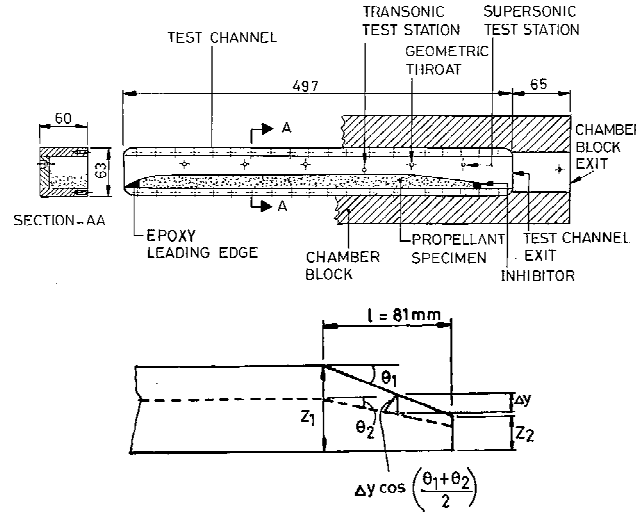

Fig. 2 Test channel assembly and burning-surface movement at the supersonic test station.

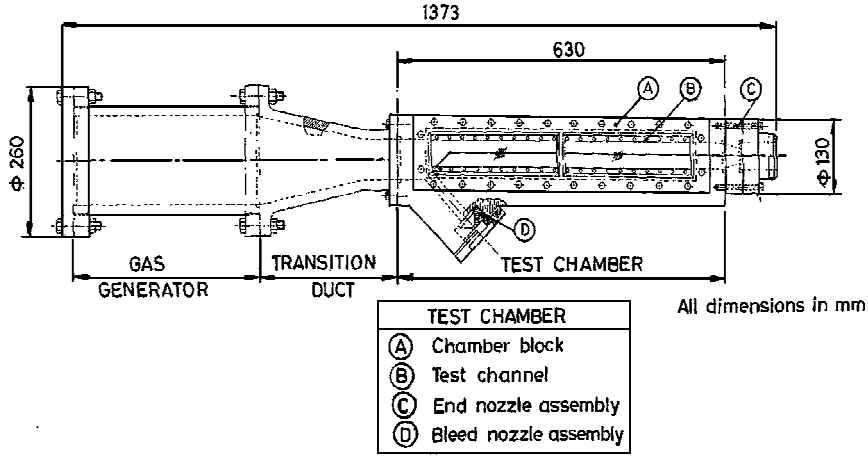

Fig. 1 Erosive burning test rig assembly.

are at 1) the head end of the gas generator; 2) upstream of the bleed nozzle; 3) four places along the test channel, i) a subsonic location, ii) the transonic test station, ($M \cong 0.8$), iii) the geometric-throat station, and iv) the supersonic test station (the six small circular holes shown in Fig. 2 above the propellant specimen are the possible pressure-tap points); and 4) just upstream of the chamber-block exit. For the vertical space available in the supersonic region, only one pressure port could be provided. However, because this port is located sufficiently downstream of the geometric throat and bottom corner in the fully expanded flow (65 mm downstream of the throat in the 81-mm length of supersonic expansion), the error due to the overestimate in static pressure may not be substantial. Recall that the end-nozzle assembly is not fitted for the nozzleless mode of testing, and, hence, the pressure just upstream of the chamber-block exit closely represents the static pressure at the jet-exit plane.

Strain-gauge-type pressure transducers (Hottinger Baldwin Messtechnik) are used for pressure measurements. During a test, all of the signals from the pressure transducers with respect to time (pressure-time records) are logged into a personal computer by the use of a data-acquisition system at a sampling rate of 200 samples per second per channel.

For a typical test run, the logging in of the pressure transducers' data with respect to time is first turned on. Subsequently, the high-speed camera is started. The camera, through an event-trigger circuit, triggers the ignition with a suitable time delay, that is, after the camera accelerates close to the steady speed. The event-trigger circuit registers the ignition pulse, as a common time signal, on the film, as well as into the pressure-time records. This common time signal helps in synchronizing the visual record of the high-speed camera with the pressure-time records. The exposed film, having the visual record of the burning, the time-interval spots, and the ignition pulse, is subsequently processed and analyzed frame by frame with a motion analyzer (L-W International).

The burning rates at the transonic test station and geometric throat are calculated based on the movement of the average burning surface, exactly below the test-station pressure port. The average surface is formed by taking three points below the test-station pressure port, separated by 10 mm: The first point on the burning surface is exactly below the pressure port, and the other two points are on either side of the first point. At the supersonic test station, the measurement of the burning-surface movement is different. This is because the burning surface in the supersonic region has the ramp angle θ. This angle changes with time due to the substantially different burning rates at the geometric throat and the supersonic exit station (Fig. 2). Hence, the flame front movement perpendicular to itself just below the supersonic test station $= \Delta y \cos(\theta_1 + \theta_2)/2$. From the projected frames, Δy can be measured directly. The change in exit ramp angle θ_1–θ_2 for a particular duration Δt is found by measuring the distances z_1 and z_2 between the two instants (Fig. 2). After the instantaneous total burning rates r are measured at the three stations, the corresponding normal-burning rates r_0 are calculated by the use of Eq. (1). Thus, the erosive burning ratios ε_b are calculated for the measured static pressures at the transonic test station, geometric-throat station, and supersonic test station.

After having calculated the ε_b with respect to time, we now have to estimate the corresponding crossflow properties: mass flux, Mach number, and velocity. The geometric-throat station remains choked for about one-half of the time of the testing duration, and the erosive burning measurements are all well within this time. As the static pressure at the geometric-throat station p_{GT} is measured, the corresponding total pressure for the choked condition $p_{0\mathrm{GT}}$, is given by,

$$p_{0\mathrm{GT}} = p_{\mathrm{GT}}[(\gamma + 1)/2]^{\gamma/(\gamma - 1)} \tag{2}$$

The static pressures are measured with respect to time, also at the transonic and supersonic test stations (p_{TT} and p_{ST}, respectively). The Mach numbers at these two stations (M_{TT} and M_{ST}) with respect to time can, therefore, be calculated if the total-pressure values ($p_{0\mathrm{TT}}$ and $p_{0\mathrm{ST}}$) are estimated. To estimate these values, the predicted head-end pressure–time trace from an internal ballistics code is matched with the experimentally obtained head-end pressure–time trace. Then, from the results of the code, the total pressure ratio between transonic test station and geometric-throat station ($R_{\mathrm{TT}} \equiv p_{0\mathrm{TT}}/p_{0\mathrm{GT}}$) and that between geometric-throat station and supersonic test station ($R_{\mathrm{ST}} \equiv p_{0\mathrm{GT}}/p_{0\mathrm{ST}}$) are noted as functions of time to calculate $p_{0\mathrm{TT}}$ and $p_{0\mathrm{ST}}$. From the total-to-static pressure ratios vs time thus obtained at the two test-stations, Mach number vs time can be calculated, as

$$(p_0/p)_{\text{test station}} = \left\{1 + [(\gamma - 1)/2]M^2_{\text{test station}}\right\}^{\gamma/(\gamma - 1)} \tag{3}$$

where, at the test station, the total pressure is an estimated one, and the static pressure is a measured one. Once M at the test station is calculated, the related velocity and mass flux are known. The internal ballistics code is briefly explained in the next section. For further details on data reduction, see Ref. 21.

It is also possible to calculate the crossflow properties by the use of a different method. From the measured positions of the burning surface, the flow areas vs time and location along the test channel can be obtained. From the total pressures at the head end and bleed, along with static pressures along the test channel, the mass flow rates can be estimated. From these, one can calculate mass flux, Mach number, and velocity. The results obtained through this method were checked against those of the preceding method for accuracy.

Internal Ballistics Code

Figure 3 schematically represents the nozzleless mode of operation of the erosive-burning test rig. The ballistics code uses the conventional incremental analysis[22,23]; but the main difference here lies in that the choking station is fixed in the grain-port passage. The analysis assumes a quasi-steady, one-dimensional, frictionless flow of combustion products with the instantaneous mass addition, having no velocity component parallel to the crossflow. It is also assumed that the products of combustion obey the perfect gas law and that the erosive burning-test rig is an adiabatic system with total temperature T_0 taken to be the adiabatic flame temperature. The specific heat ratio and molecular mass are assumed to be constant throughout the flow. By design, the propellant loading fraction in the gas generator is low at 0.7, and the ratio of grain exit-port-area to geometric-throat area is high at 5. Therefore, a uniform total pressure p_{01} is assumed to prevail for the entire gas generator. At time $t = 0$, the approximate head-end pressure p_{01} is estimated from Eq. (4):

$$P_{01} = \left(\rho_p a K c^*\right)^{[1/(1-n)]} \tag{4}$$

where

$$K = \left(\frac{A_{\mathrm{bg}} + A_{\mathrm{bs}}}{A_t + A_{\mathrm{tb}}}\right) \tag{5}$$

Here, A_{bg} is gas generator grain burning area, A_{bs} is the surface area of specimen propellant, A_t is the area of geometric throat section, A_{tb} is the bleed-nozzle throat area. Note that c^* is the characteristic velocity and ρ_p is the propellant density.

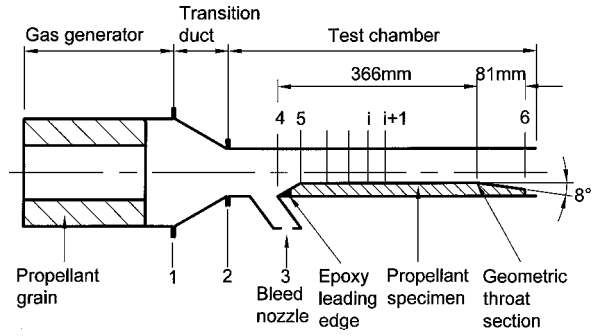

Fig. 3 Erosive burning test rig operating in nozzleless mode.

The mass flow rate of burned products $\dot{m}$ from the gas generator is given by

$$\dot{m} = \rho_p A_{bg} a p_{01}^n \tag{6}$$

For this mass flow rate passing through station 2 (Fig. 3), by mass conservation, M_2 is given by

$$\dot{m} = \frac{\sqrt{\gamma/RT_{02}}A_2 K_1 P_{01} M_2}{\left\{1 + [(\gamma-1)/2]M_2^2\right\}^{(\gamma+1)/2(\gamma-1)}} \tag{7}$$

Here $K_1 = p_{02}/p_{01}$. The subsonic value of M_2 is calculated by iteration. The mass flow rate $\dot{m}_3$ through the bleed nozzle is given by

$$\dot{m}_3 = \frac{K_2 p_{02} A_{tb}\sqrt{\gamma}[2/(\gamma+1)]^{(\gamma+1)/2(\gamma-1)}}{\sqrt{RT_0}} \tag{8}$$

The stagnation-pressure losses in the transition duct and the bleed passage are accounted for under the assumption that $K_1 = K_2(=p_{03}/p_{02}) = 0.98$. This 4% loss in stagnation pressure closely checks with the pressure values measured at the head end and the bleed upstream. The properties at station 4 are obtained by the conservation of mass, momentum, and energy between 2 and 4. For simplicity, the mass flow passing through station 3 is taken to be bled with zero axial momentum, and the flow from stations 2 to 4 is taken as the constant area flow. Similarly, by the conservation of mass, momentum, and energy for flow with area variation and mass addition, the crossflow properties at stations 5 and downstream are obtained up to the geometric throat. In this process, the choking may occur before the geometric throat; or it may not occur at the geometric throat (the geometric throat having a subsonic flow). If the Mach number at the geometric throat is not equal to $(1-\delta)$, the head-end pressure is suitably altered, and the new Mach number distribution up to the geometric throat is calculated. This iterative procedure is continued until $M = (1-\delta)$ at the geometric throat. Numerically, $M = 1$ can not be reached at the throat, and δ is typically kept at 0.01. When this condition is satisfied, for a chosen instant, the solution of the flowfield upstream of the geometric throat is complete. Further downstream, up to station number 6, the supersonic value of Mach numbers at every step can be determined incrementally. Once the entire port flowfield is determined, the time is incremented by an interval δt. Under quasi-steady-state assumptions, the gas generator grain surface and the propellant specimen surface are made to regress as per the local gasdynamic properties under the assumed burning-rate equation. With the new burning surface configuration, the code returns to the gas generator head end to start the iteration with the p_{01} converged earlier. The resulting flowfield is computed as described earlier. The entire procedure is repeated until the test rig is unchoked.

In a flow with simultaneous area variation and mass addition, it is not mandatory that the flow should choke at the minimum area location. Once the effect due to mass addition takes over the effect due to area variation, the choking station shifts to a place where both of the effects are equal. From the influence coefficient equation of Mach number,[24]

$$(1-M^2)\frac{dM}{dx} = M\left(1 - \frac{\gamma-1}{2}M^2\right)\left\{-\frac{1}{A}\frac{dA}{dx} + (1+\gamma M^2)\frac{1}{\dot{m}}\frac{d\dot{m}}{dx}\right\} \tag{9}$$

At $M = 1$, the term in brace brackets becomes equal to zero:

$$\left\{-\frac{1}{A}\frac{dA}{dx} + (1+\gamma M^2)\frac{1}{\dot{m}}\frac{d\dot{m}}{dx}\right\} = 0 \tag{10}$$

Therefore,

$$\frac{dA}{dx} = A(1+\gamma M^2)\frac{1}{\dot{m}}\frac{d\dot{m}}{dx} \tag{11}$$

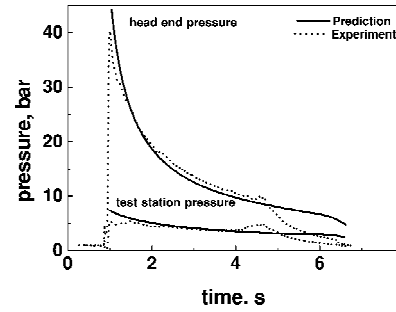

Fig. 4 Predicted pressure time trace with experimental pressure time trace at head end and supersonic test station (test number 33).

Because the right-hand side of Eq. (11) is positive, the flow should choke somewhere in the nozzle passage where $dA/dx > 0$. The location of the choking station is fixed by solving Eq. (10).

The burning-rate equation assumed here is that of Lenoir and Robillard,[25]

$$r = ap^n + \frac{\alpha G^{0.8}}{L^{0.2} e^{(\beta r \rho_p / G)}} \tag{12}$$

where L is the length from the leading edge of the specimen propellant, G the mass flux of crossflow, and α is a constant that is calculated internally by,

$$\alpha = \frac{0.0288 c_p \mu^{0.2} Pr^{-0.667}}{\rho_p c_{ps}} \frac{(T_0 - T_s)}{(T_s - T_i)} \tag{13}$$

and β is a given dimensionless constant that depends on a specific propellant. Here μ and Pr are the viscosity and Prandtl number of the combustion products, whereas c_{ps} and T_i are the specific heat and initial temperature of the propellant. The surface temperature of the propellant T_s is estimated from the equation given by Draskovic et al.[26]

The Lenoir–Robillard equation does not account for negative erosive burning. Although, in the present study, negative erosive burning is observed locally under certain operating conditions, the overall application of the Lenoir–Robillard equation for the code is taken to be acceptable because the code is used only to estimate the extent of total pressure loss between the transonic test station and the geometric throat and between the geometric throat and the supersonic test station. Under negative erosive burning, the local stagnation pressure losses due to mass addition will be slightly less than the ones predicted by the code.

Figure 4 shows the comparison of the predicted pressure–time trace with the experimental one at the head end, as well as with the supersonic test station (431 mm from the leading edge of the specimen propellant). In this prediction, the value of α is calculated by the use of Eq. (13), and β is obtained by trial and error fitting. A good match is obtained for a β value of 90.

Uncertainty Level and Error Analysis

Every frame of the film, having the visual record of the burning surface, is projected on to the motion-analyzer screen at a magnification of four (beyond this magnification, the view becomes hazy). For this projection, the minimum discernible flame front movement is 0.125 mm. Consequently, the uncertainty in the measurement of burning-surface movement rate is found to be $\pm 7.5\%$. These values are repeatable within $\pm 6\%$. Therefore, the uncertainty in the total burning rate is less than $\pm 10\%$. Uncertainty in the normal burning rate is $\pm 3.5\%$, and this leads to the uncertainty in the measurement of an ε_b of around $\pm 10\%$. Note that the geometric throat is choked for the duration of measurements. Thus, with the pressure transducers of accuracy $\pm 0.1\%$, the uncertainty in the value of p_{0GT} is also within $\pm 0.1\%$. Through the internal ballistics code, generally reasonable matches of static pressures at the transonic test station and the supersonic test station are obtained. For an uncertainty of $\pm 7.5\%$ in R_{TT} and R_{ST}, the uncertainty in the transonic test-station Mach number, $M_{TT}(\approx 0.8)$, is within $\pm 10\%$. The Mach number at the supersonic test station M_{ST} varies from 1.7 to 1.2, and the uncertainty for these values is found to vary, respectively, from ± 3 to $\pm 5\%$.

Results and Discussion

Three different propellants of the same fractions of composition [AP: HTPB: di-2-ethyhexyl adipate (DOA): toluene-di-isocynate (TDI) = 0.7300: 0.2160: 0.0405: 0.0135], but of different burning rates (6, 9, and 16 mm/s at 5 MPa) were used for the study. The first propellant, denoted formulation 1, contained AP particles of mass mean diameter,

$$d_{4,3}\left\{ \equiv \left[\sum \left(n_i d_i^4 \right) \Big/ \sum \left(n_i d_i^3 \right) \right] \right\}$$

of 100 μm. Both the second and the third propellants, denoted formulations 2 and 3, respectively, contained AP particles of $d_{4,3} = 20$ μm. However, the formulation 3 contained 2% copper chromite catalyst, and the balance 98% contained the fractions of composition just mentioned.

Table 1 lists the propellant characteristics. Adiabatic flame temperature, molecular mass, and the ratio of specific heats of the combustion products were calculated with the code NASA CEC71.[27] In the internal ballistics calculations, neglected for the formulation 3 (with respect to the other two formulations) were the small changes that would result in the values of ρ_p, T_0, γ, and molecular mass of the combustion products due to the addition of the copper chromite catalyst. The normal-burning rate characteristics of the propellants were determined for a pressure range of 0.5–6.5 MPa by the use of a chimney-type strand burner. Measured normal-burning rate data are given in Fig. 5. The fitted burning-rate equations for the three formulations are given in Table 1.

When the erosive burning test facility was realized, the first study undertaken was a study of erosive burning under subsonic crossflow conditions (nozzled mode). Under this nozzled mode, there were many failures, primarily due to the leakage through the sacrificial layer. With a modified design for the assembly of the sacrificial layer with the test channel, the confidence level improved. There were no total failures of any test under the nozzleless mode of testing, though a few tests were not repeatable; the success rate was around 80%. Table 2 gives the details of the erosive-burning tests conducted. The last column of Table 2 indicates the pairs of repeated tests.

Figure 6 shows the views clipped from the S-Video recording of a nozzleless mode of operation. Toward the end of burning, the ramp surface along the supersonic expansion becomes almost parallel to the test channel. This indicates that the propellant burns faster in the throat region than along the ramp.

In nozzleless motors, as the chamber stagnation pressure keeps falling with time, concern always exists as to whether the supersonic port passage will overexpand, endangering flow separation. Quantification of erosive-burning rates at the geometric throat and in the supersonic region would resolve this concern. However, it is encouraging that, under this situation, the total burning rate at the geometric throat is always greater (enhanced burning rate due to higher static pressure, despite lower ε_b) than that in the supersonic region (reduced burning rate due to lower static pressure despite higher ε_b). This results in the reduction of supersonic area ratio with respect to time, thus the extent of overexpansion is reduced or removed. (Figs. 7 and 8).

Table 1 Characteristics of the propellants

Characteristics	Numerical value
Propellant density, ρ_p	1508 kg/m^3
Adiabatic flame temperature of combustion products, T_0	1730 K
Average molecular mass of combustion products	19.25 kg/kgmol
Ratio of specific heats of combustion products, γ	1.295
Formulation 1 (AP, 100 μm), burning rate, m/s[a]	$r_0 = 3.3 \times 10^{-6}\ p^{0.49}$
Formulation 2 (AP, 20 μm), burning rate, m/s[a]	$r_0 = 5.6 \times 10^{-5}\ p^{0.33}$
Formulation 3 (AP, 20 μm), burning rate, m/s[a]	$r_0 = 6.22 \times 10^{-5}\ p^{0.36}$

[a]Variable p in pascal.

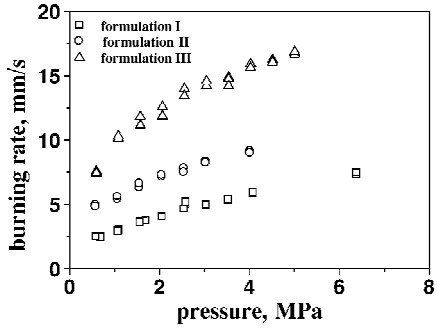

Fig. 5 Burning rate at zero crossflow velocity for the three formulations obtained from strand burner.

Table 2 Erosive burning test conditions

Specimen propellant formulation	Gas generator propellant formulation	Specimen thickness, mm	Maximum gas generator pressure, MPa	Repeated pairs of test numbers
1	1	21	1.2	30, 31
1	1	27	2.0	32, 35
1	2	27	4.5	33, 34
2	1	27	3.0	37, 39
2	2	27	6.5	36, 38
3	1	27	3.3	41, 42
3	2	27	5.0	40, 43

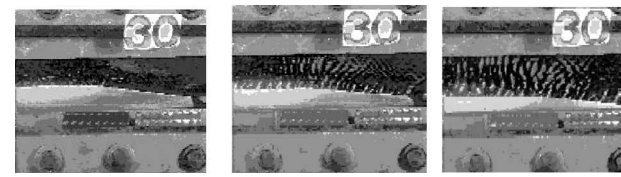

a) b) c)

Fig. 6 Erosive burning under transonic and supersonic crossflow Mach numbers: a) first second, b) third second, and c) fifth second (the flow is from left to right), test number 30.

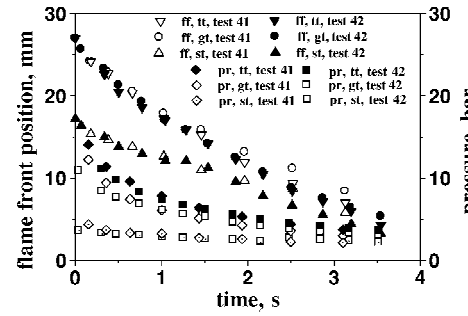

Fig. 7 Flame front positions and static pressures with respect to time from two repeatable tests for formulation 3 propellant with the synchronized pressure: flame front (ff), transonic test station (tt), geometric throat (gt), supersonic test station (st), and pressure (pr).

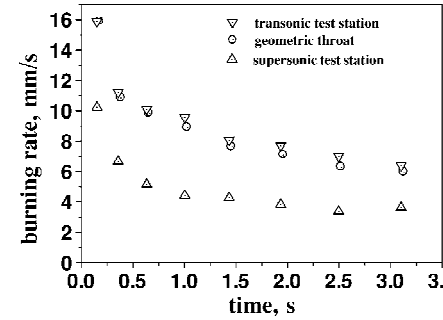

Fig. 8 Burning rate at transonic test station, geometric throat, and supersonic test station vs time (formulation 3 and test number 41).

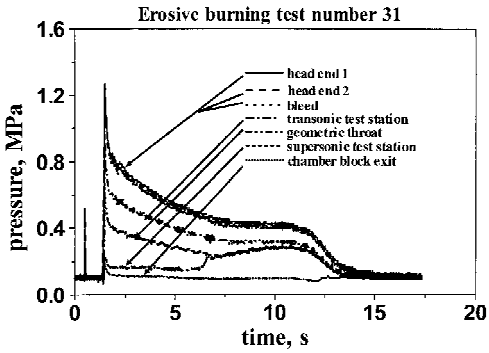

Fig. 9 Pressure time trace of a nozzleless test.

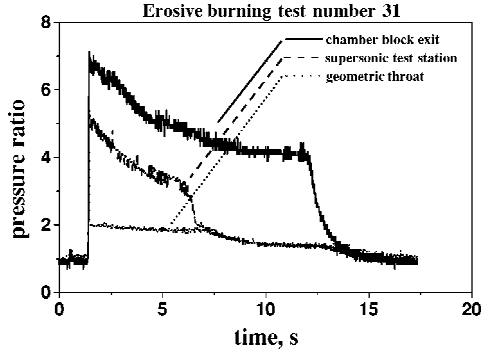

Fig. 10 Pressure ratio vs time of a nozzleless test.

Choking Station Movement

As indicated earlier, it is not mandatory for the flow always to choke at the geometric throat. Figure 9 shows the pressure–time records of a typical nozzleless test. The clustered top band actually represents a set of three traces: the head ends 1 and 2 and the bleed. The traces of head ends 1 and 2 almost overlap each other. Because of the stagnation pressure loss from the head end to the bleed, the pressure trace of the bleed is the lowest. All of the pressures, except those at the supersonic test station p_{ST} and the one just upstream of the chamber-block exit p_e (the two bottommost traces), are visibly regressive up to about $6\frac{3}{4}$ s. At the supersonic test station, after the initial peak, the pressure remains almost constant up to about $6\frac{1}{4}$ s and starts rising to merge with that at the geometric throat at around $6\frac{3}{4}$ s, indicating the crossing of the choked station. The two pressures (those at the geometric throat as well as at the supersonic test station) that are about equal after $6\frac{3}{4}$ s and, hence, appear merged, proceed to rise slowly up to about 10 s, to remain constant up to around 11 s, and then to start to tail off. Also, p_e, after its initial peak, is slightly above atmospheric pressure and remains almost constant for the entire test duration, indicating an underexpanded supersonic flow at the chamber-block exit. All of the curves start to tail off at the burnout that occurs at around 11 s.

Figure 10 shows that with respect to time, the ratios of the pressure upstream of the bleed nozzle p_b to that at the stations referred to at three different locations: 1) the geometric throat, 2) the supersonic test station, and 3) just upstream of chamber-block exit. At the point of pressure measurement upstream of the bleed nozzle, the Mach number is much less than 0.2, and, therefore, p_b can be taken as the stagnation value. The exit pressure ratio (p_b/p_e) goes below the choking value of around 1.9 after approximately 13 s. Therefore, the station just upstream of chamber-block exit had supersonic flow almost for the entire duration of the test. At the geometric throat, the flow is choked up to $6\frac{1}{4}$ s. At around $6\frac{3}{4}$ s, the same flow is unchoked to momentarily choke the flow at the supersonic test station downstream. Correspondingly, the supersonic test station pressure ratio (p_b/p_{ST}) is sufficiently above 3 up to $6\frac{1}{4}$ s. It then starts falling and falls below 1.9 after $6\frac{3}{4}$ s. This indicates that the choking location is moving past the supersonic test station at around $6\frac{3}{4}$ s. After $6\frac{3}{4}$ s, the station has a subsonic flow. After $6\frac{3}{4}$ s, the choking location shifts to the test-channel exit (Fig. 2). This is predictable because the traces of upstream stagnation pressures (head end and bleed) are essentially constant from $6\frac{3}{4}$ s to $11\frac{1}{2}$ s (Fig. 9), as is the pressure ratio at the chamber-block exit, $p_b/p_e > 4$, which is far above the choking value. After the choking station shifts to the test-channel exit, the static pressures at the geometric throat and the supersonic test station are nearly equal. (The distance between these two stations is only 65 mm.) This corresponds to a subsonic flow at the two stations. As the propellant slab recedes, enlarging the port-flow area, the two static pressures continue to increase (Fig. 9) because of the fall in subsonic Mach numbers there.

Erosive Burning at Supersonic Conditions

For a typical test, the measurements of total burning rates at the transonic test station, geometric throat, and supersonic test station are shown in Fig. 11. The highest burning rate for each station almost corresponds to the burning rates at the beginning of the test. As time proceeds, the burning rates decrease due to the fall in pressure and mass flux. For the choked duration at the geometric throat, the velocity and Mach number are constant with respect to time, but the pressure keeps falling. Therefore, in the nozzleless mode of firing at the geometric throat, erosive-burning data are measured at a constant velocity or Mach number of unity for a wide variation in pressure and mass flux.

Figures 12 and 13 show the measured supersonic test-station pressures and burning rates for two pairs of repeated tests, one for formulation 1 propellant and the other for formulation 3.

At the transonic, sonic, and supersonic test stations, for each of the 14 erosive-burning tests (Table 2), we have pressures (static as well as total), total burning rates r, normal-burning rates r_0, Mach numbers (or equivalent velocities), and mass fluxes with respect to time.[28] When Mach numbers are chosen as parameters, r and r_0 can be obtained with respect to static pressure. Figures 14–16 depict the corresponding points for the three formulations. A summary of all of the tests is given in Fig. 17. The interpolation procedure adopted to obtain the points has further increased the dispersions.

In subsonic crossflow conditions, the erosive-burning effect generally increases with an increase in both the pressure and freestream velocity of the crossflow. Also, the propellants with lower normal-burning rates experience greater erosive burning than those with

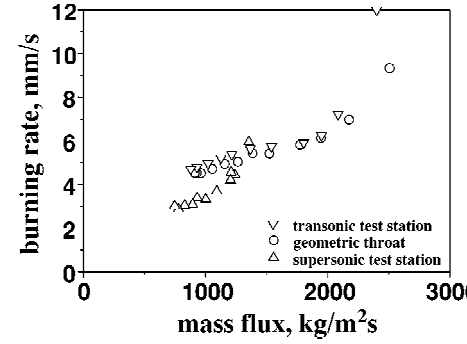

Fig. 11 Burning rate vs mass flux for test number 33.

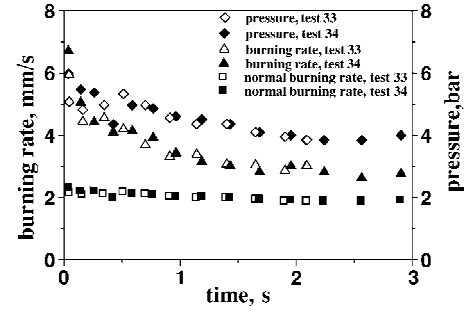

Fig. 12 Burning rate, normal-burning rate, and static pressure at supersonic test station with time of two repeatable tests (tests 33 and 34) of propellant formulation 1.

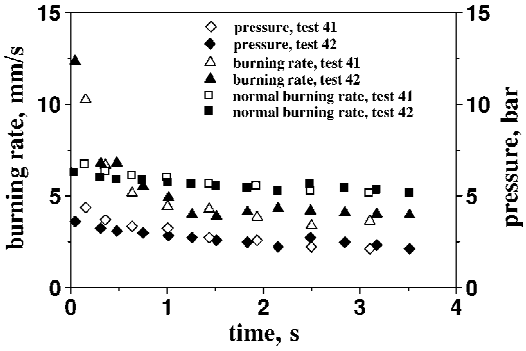

Fig. 13 Burning rate, normal-burning rate, and static pressure at supersonic test station with time of two repeated tests (tests 41 and 42) of propellant formulation 3.

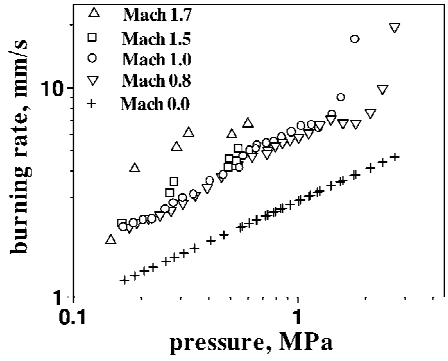

Fig. 14 Burning rate vs pressure at various crossflow Mach numbers for formulation 1 (test numbers 30–35).

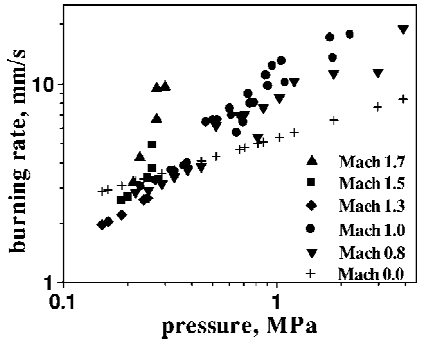

Fig. 15 Burning rate vs pressure at various crossflow Mach numbers for formulation 2 (test numbers 36–39).

higher normal-burning rates. The present results also demonstrate these characteristics in supersonic conditions. With the reduction in pressure, the total burning rates of the formulations 2 and 3 attain and go below the corresponding normal-burning rates, demonstrating negative erosive-burning rates in supersonic crossflow conditions (Figs. 13, 15, and 16).

The occurrence of supersonic negative erosive burning only in low pressures should not be thought of as not practically relevant to actual motor conditions. In the supersonic expansion region of the grain ports of nozzleless motors, low pressures do occur during a significant portion of the effective thrusting time.

In subsonic crossflow conditions, negative erosive-burning rates have been reported for both composite and double-base propellants.[4–6,9,13] However, there is some controversy as to the cause for the negative erosive burning.

The experimental result of Zucrow et al.[9] indicated negative erosive burning. Zucrow et al. attributed the phenomenon to the consequence of the predominant effect of decreasing convective heat transfer to the propellant surface caused by mass blowing into the boundary layer. (See Fig. 12 of Ref. 29.) Their line of reasoning runs as follows: Within the region of negative erosive burning, up to the

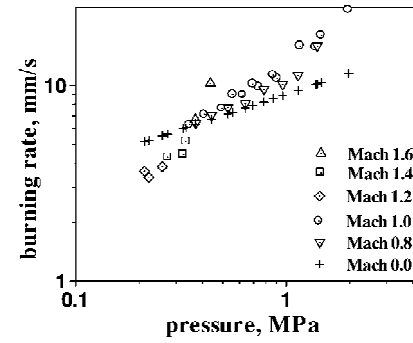

Fig. 16 Burning rate vs pressure at various crossflow Mach numbers for formulation 3 (test numbers 40–43).

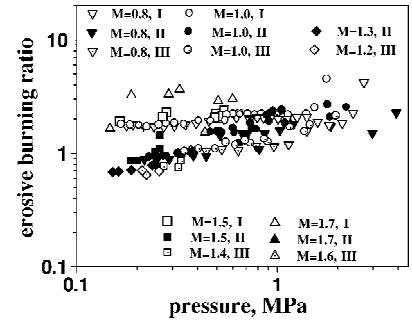

Fig. 17 Erosive burning ratio vs pressure at various crossflow Mach numbers of the three formulations, 1, 2, and 3 (test numbers 30–43).

point of maximum negative erosive burning (minimum of $\varepsilon_b < 1$) the mass blowing into the boundary layer predominates. Beyond this point, the effect due to convective heat transfer becomes significant, and, at the threshold velocity, this convective effect nullifies the mass blowing effect (in reducing the heat transfer to the propellant surface). Above the threshold velocity, the convective heat transfer to the propellant surface predominates and, thus, causes the positive erosive burning. However, King[19] shows that the prediction of negative erosive burning by the use of this concept results from impractical physical situations.

Vilyunov and Dvoryashin[6] were the first to identify and discuss the behavior of negative erosive burning in 1971 and later confirmed it by a specific experimental procedure.[30] The propellants used were of double base, as well as composite types. Vilyunov and Dvoryashin[6] attributed the negative erosive burning to the structure of the turbulent flow and its effect on the transport properties and the reaction rate. They argued that the negative erosive burning could occur either due to the decrease in reaction rate in the presence of large-scale turbulence or due to the inequality of the transport coefficients in the case of small-scale turbulence. Following the results of Ref. 6, there have been some modeling efforts on negative erosive burning by Russian researchers.[17,31,32] Among these efforts, the latest one[17] is for the region where the boundary layer is not fully developed (low Reynolds number). This is because, as per these authors, the physical mechanism of negative erosive burning is based on the premise that the turbulence does not have any effect. Hence, when the laminar flow over the surface is not fully developed, the additional convective heat transfer due to the higher crossflow-velocity gradient pushes the flame zone away from the burning surface. As a result, the heat flux from the pushed flame zone into the solid propellant decreases. Therefore, the burning rate drops, resulting in negative erosive burning. Contrary to the basic physical mechanism assumed for this model,[17] the negative erosive burning observed in the present study is not over the region where the flow has yet to be developed. When the characteristic dimension for the channel flow in the test section is taken to be the hydraulic diameter, its average value is 132 mm. For this, at $M = 1.6$ and pressure = 0.3 MPa, and with $\mu = 9.3 \times 10^{-5}$ kg/m · s, the Reynolds number is around 10^6.

Negative erosive burning can be found in additive-modified double-base propellants of super burning rates and plateau-burning

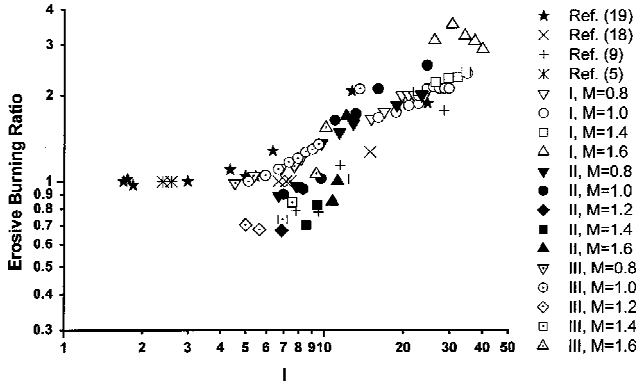

Fig. 18 Plot of erosive-burning ratio vs the nondimensional parameter I for subsonic, sonic, and supersonic crossflow Mach numbers.

composite propellants.[33,34] The former cause is attributed to the shearing away of superrate-producing carbon residues by the crossflow.[33] The latter cause is attributed to the "stifling" of the propellant combustion by the flow of melted binder across the oxidizer crystals.[34] However, the propellants studied by Zucrow et al.,[9] Peretz,[5] and the present investigators are nonplateau-burning composite propellants.

Recent modeling efforts[19] do not include negative erosive burning. More importantly, these are not based on the alteration of convective heat transfer from the crossflow, but on that of transport properties in the region between the gas flame and the propellant surface. The alteration of transport properties, leading to the change in heat flux to the propellant surface, are generally calculated based on turbulence effects. The model by Godon et al.[18] and Lengellé,[34] which falls under this category, is shown to predict the general characteristics of positive erosive burning, the threshold mass flux, and the scale effects.

A nondimensional parameter I, proposed by Vilyunov in 1961 to characterize erosive burning should be mentioned at this juncture.[6] It is defined as

$$I \equiv (\rho u/\rho_p r_0)\sqrt{\xi} \tag{14}$$

where ρu is the crossflow mass flux and ξ is the resistance coefficient. Vilyunov and Dvoryashin[6] experimentally showed that the erosive burning ratio ε_b increased with I beyond a threshold value of I at which $\varepsilon_b = 1$. They demonstrated that below a threshold value of 5.6, negative erosive burning could occur. However, based on subsequent studies conducted by Russian researchers,[17,31,32] it appears that the threshold value of 5.6 cannot be taken as the universal criterion for prediction of negative erosive-burning features. However, it seems that at low values of I the threshold is reached, and the exact value of I at the threshold is system dependent. Also, at the values of I below the threshold value, certain propellants can demonstrate negative erosive burning. The erosive-burning data of the present study, as well as those from other studies[5,9,18,19] appear to be consistent with this behavior (Fig. 18). Among the results of the other studies,[5,9,18,19] only Ref. 9 gives experimental points for negative erosive burning. Although Peretz[5] observed negative erosive burning, he indicated only the threshold mass flux below which the negative erosive burning was observed.

In addition to the possible correlation of ε_b, the nondimensional parameter I is seen to predict scaling and burning rate effects reasonably. The resistance coefficient ξ in the first approximation is given by the Blasius formulas as equal to $0.3164Re^{-0.25}$. Equation (14) can now be written as

$$I = \sqrt{0.3164}\left[(\rho u)^{\frac{7}{8}}/(\rho_p r_0)\right](\mu/D)^{\frac{1}{8}} \tag{15}$$

where μ is the viscosity of combustion products and D is the characteristic dimension of the grain port. If we assume, as projected, that the threshold mass flux is attained for a particular value of I, the threshold mass flux is seen to be proportional to $D^{1/7}$ with respect to the scale effect and to $r_0^{8/7}$ with respect to the effect of a normal-burning rate. The values calculated for typical situations closely match with those predicted by the model by Godon et al.[18] and Lengellé.[34]

Conclusions

An experimental facility was developed to measure erosive-burning rates under supersonic crossflow conditions. As observed under subsonic crossflow conditions, in supersonic conditions the following conditions hold: 1) The erosive burning effect increases with the increase in both pressure and freestream velocity of crossflow. 2) The propellants with lower normal-burning rates experience greater erosive burning than those with higher normal-burning rates. The experimental procedure adopted facilitated a clear demonstration of choking station movement in the grain port of nozzleless motors. Negative erosive burning under supersonic crossflow conditions is identified under low-pressure conditions, and it is found to be more significant for faster burning propellants.

Acknowledgments

The present work forms a part of the research sponsored by the Aeronautics Research and Development Board, Ministry of Defence, Government of India through the sanction numbers AERO/RD-134/100/10/90-91/643 and AERO/RD-134/100/10/96-97/929. The film motion analysis was done at the Hydroturbomachines Laboratory, Department of Mechanical Engineering, Indian Institute of Technology Madras, Chennai, India. The Igniter and Pyrotechnic Group in the Vikram Sarabhai Space Centre of the Indian Space Research Organisation (ISRO) designed the igniter and Sriharikota Range Centre of ISRO supplied HTPB, DOA, and TDI for the experiments.

References

[1] Vandenkerckhove, J., and Jaumotte, A., "Remarks on the Burning Mechanism and Erosive Burning of Ammonium Perchlorate Propellants," *Eighth Symposium (International) on Combustion*, Williams and Wilkins, Baltimore, MD, 1962, pp. 689–692.

[2] Razdan, M. K., and Kuo, K. K., "Measurements and Model Validation for Composite Propellants Burning Under Crossflow of Gases," *AIAA Journal*, Vol. 18, No. 6, 1980, pp. 669–677.

[3] Green, Jr., L., "Erosive Burning of Some Composite Solid Propellants," *Jet Propulsion*, Vol. 24, No. 1, 1954, pp. 9–15, 26.

[4] Marklund, T., and Lake, A., "Experimental Investigation of Propellant Erosion," *ARS Journal*, Vol. 3, No. 2, 1960, pp. 173–178.

[5] Peretz, A., "Experimental Investigation of the Erosive Burning of Solid Propellant Grains with Variable Port Area," *AIAA Journal*, Vol. 6, No. 5, 1968, pp. 910–912.

[6] Vilyunov, V. N., and Dvoryashin, A. A., "An Experimental Investigation of the Erosive Burning Effect," *Combustion Explosion and Shock Waves*, Vol. 7, No. 1, 1971, pp. 38–42.

[7] Samusev, V. F., and Umblia, S. B., "Erosion Combustion of Ballistic Powders," *Combustion Explosion and Shock Waves*, Vol. 13, No. 3, 1976, pp. 393, 394.

[8] Kamath, H., Aroara, R., and Kuo, K. K., "Erosive Burning Measurements and Predictions for a Highly Aluminized Composite Solid Propellant," AIAA Paper 82-1111, June 1982.

[9] Zucrow, M. J., Osborn, J. R., and Murphy, J. M., "An Experimental Investigation of the Erosive Burning Characteristics of a Nonomogeneous Solid Propellant," *AIAA Journal*, Vol. 3, No. 3, 1965, pp. 523–525.

[10] Razdan, M. K., and Kuo, K. K., "Turbulent Flow Analysis and Measurements of Erosive Burning Rates of Composite Solid Propellants," AIAA Paper 80-1209, June 1980.

[11] Burick, R. J., and Osborn, J. R., "Erosive Combustion of Double Base Solid Rocket Propellants," Chemical Propulsion Information Agency, CPIA Publication 162, Vol. 2, Laurel, MD, 1967, pp. 57–69.

[12] King, M. K., "Erosive Burning of Composite Solid Propellants: Experimental and Model Studies," *Journal of Spacecraft and Rockets*, Vol. 16, No. 3, 1979, pp. 154–162.

[13] Dickinson, L. A., Jackson, F., and Odgers, A. L., "Erosive Burning of Polyurethane Propellants in Rocket Engines," *Eighth Symposium (International) on Combustion*, Williams and Wilkins, Baltimore, MD, 1960, pp. 754–759.

[14] Lawrence, W. J., Mathews, D. R., and Deverall, L. I., "The Experimental and Theoretical Comparison of the Erosive Burning Characteristics of Composite Propellants," AIAA Paper 68-531, June 1968.

[15]Viles, J. M., "Measurement of Erosive Burning Rates," Rohm and Hoas Company, TR 5-213, Huntsville, AL, Jan. 1969.

[16]Rout, R. K., Mukunda, H. S., and Jain, V. K., "Erosive Burning Characteristics of Solid Propellant Rocket Motor," AIAA Paper 78-1097, July 1978.

[17]Bulgakov, V. K., Karpov, A. I., and Lipanov, A. M., "Numerical Studies of Solid Propellant Erosive Burning," *Journal of Propulsion and Power*, Vol. 9, No. 6, 1993, pp. 812–818.

[18]Godon, J. C., Duterque, J., and Lengellé, G., "Erosive Burning in Solid Propellant Motors," *Journal of Propulsion and Power*, Vol. 9, No. 6, 1993, pp. 806–811.

[19]King, M. K., "Erosive Burning of Solid Propellants," *Journal of Propulsion and Power*, Vol. 9, No. 6, 1993, pp. 785–805.

[20]Mukunda, H. S., and Paul, P. J., "Universal Behaviour in Erosive Burning of Solid Propellants," *Combustion and Flame*, No. 1/2, Vol. 109, 1997, pp. 224–236.

[21]Krishnan, S., and Rajesh, K. K., "Experimental Investigation of Erosive Burning of Composite Propellants Under Supersonic Crossflows," *Combustion of Energetic Material: Proceedings of the 5th International Symposium on Special Topics in Chemical Propulsion (5-ISICP)*, edited by K. K. Kuo and L. T. DeLuca, Begal House Inc., New York, 2002, pp. 316–329.

[22]"Solid Propellant Rocket Motor Internal Ballistics Program," Vol. 1, The Boeing Company, Seattle, WA, 1967.

[23]Miller, W. H., and Barrington, D. K., "A Review of Contemporary Solid Rocket Motor Performance Prediction Techniques," *Journal of Spacecraft and Rockets*, Vol. 7, No. 3, 1970, pp. 225–237.

[24]Shapiro, A. H., *The Dynamics and Thermodynamics of Compressible Fluid Flow*, Vol. 1, Ronald, New York, 1953, pp. 219–262.

[25]Lenoir, J. M., and Robillard, G., "A Mathematical Method to Predict the Effects of Erosive Burning in Solid Propellant Rockets," *Proceedings of the Sixth Symposium (International) on Combustion*, Reinhold Publishing Corp., New York, 1957, pp. 663–667.

[26]Draskovic, D., Jojic, B., Balagojevic, D., and Adzic, M., "The Practical Method of Determining Erosive Burning Rate of Solid Rocket Propellant," *29th International Astronautical Conference*, Dubrovnik, Yugoslavia, 1978; also International Aeronautics Federation, Paper IAF-78-227.

[27]Gordon, S., and McBride, B. J., "Computer Program for Calculation of Complex Chemical Equilibrium Compositions, Rocket Performance, Incident and Reflected Shocks, and Chapman–Jouguet Detonations," NASA SP-273, 1971.

[28]Rajesh, K. K., "Erosive Burning Studies of Composite Propellants Under Transonic and Supersonic Crossflow Mach Numbers," Ph.D. Dissertation, Dept. of Aerospace Engineering, Indian Inst. of Technology Madras, Chennai 600036, India, Sept. 1999.

[29]Razdan, M. K., and Kuo, K. K., "Erosive Burning of Solid Propellants," *Fundamentals of Solid Propellant Combustion*, edited by K. K. Kuo and M. Summerfield, Vol. 90, Progress in Astronautics and Aeronautics, AIAA, New York, 1984, pp. 515–598.

[30]Vilyunov, V. N., and Dvoryashin, A. A., "Effect of the Initial Temperature of a Condensed Substance on the Value of Negative Erosion," *Combustion, Explosion, and Shock Waves*, Vol. 9, No. 4, 1973, pp. 521, 522.

[31]Bulgakov, V. K., and Lipanov, A. M., "Model of the Combustion of Solid Fuel with Blowoff, Taking Account of the Interaction of Turbulence with the Chemical Reaction," *Combustion, Explosion, and Shock Waves*, Vol. 20, No. 5, 1984, pp. 538–542.

[32]Bulkakov, V. K., Lipanov, A. M., Vilyunov, V. N., and Karpov, A. I., "The Negative-Erosion Mechanism in Solid-Fuel Combustion," *Combustion, Explosion, and Shock Waves*, Vol. 25, No. 4, 1989, pp. 410–412.

[33]Godon, J. C., Duterque, J., and Lengellé, G., "Solid-Propellant Erosive Burning," *Journal of Propulsion and Power*, Vol. 8, No. 4, 1992, pp. 741–747.

[34]Lengellé, G., "Model Describing the Erosive Combustion and Velocity Response of Composite Propellants," *AIAA Journal*, Vol. 13, No. 3, 1975, pp. 315–322.